Termination of BIF deposition in the Paleoproterozoic: the Tongwane Formation, South Africa

Stefan Schröder, Matthew R.Warke

Basin Studies and Petroleum Geoscience, School of Earth, Atmospheric and Environmental Sciences, University of Manchester, Manchester M13 9PL, United Kingdom, email: stefan.schroeder@manchester.ac.uk

Abstract

The Tongwane Formation (~2.4 Ga) conformably overlies banded iron formations (BIF; Penge Iron Formation) on the Kaapvaal Craton, South Africa. As such, it provides a unique window into depositional processes and environmental conditions in the aftermath of major Archean-Paleoproterozoic BIF deposition, and on the eve of irreversible environmental oxygenation in the Great Oxidation Event (GOE, ~2.35 Ga). This study presents the first sedimentological and bulk-rock geochemical characterization of the Tongwane Formation to provide a sedimentological and stratigraphic framework for further studies of early Paleoproterozoic environments.

The Tongwane Formation is 220m thick and consists from the base up of shales, siliceous mudstones with local BIF facies, interbedded mudstones and dolomites, and a massive dolomite unit at the top. Strata record the progressive shallowing of depositional environments from deep shelf (BIF) to a wave-swept carbonate ramp. Intervening slope environments record increased detrital sedimentary input in the form of shales and distal turbidites. The carbonate ramp had a distally steepened margin as documented by an important margin collapse breccia. Extension due to seismic forces and/or slope steepening caused progressive deformation of slope deposits, from slumping and fracturing through sedimentary boudinage, to brecciation, and mass wasting.

Termination of BIF deposition could have been related to (a) shutdown of Fe-precipitating processes, (b) shutdown of the hydrothermal Fe source, (c) shallowing of environments to restrict

BIF deposition to deeper parts of the basin, (d) masking of Fe deposition by increased detritus, or a combination of these. Although a partial or complete shutdown of the Fe source or of Fe precipitating processes cannot be excluded, the weight of evidence from the Tongwane Formation favors external factors such as relative sea level fall and Fe dilution by increased detrital input as the main drivers for the BIF-carbonate transition. All samples fall on a mixing curve between hydrothermal and detrital end members, and despite metamorphic overprint, a weak hydrothermal signature is observed up to below platform deposits. These results stress the importance of understanding sedimentary factors in studies of Archean-Paleoproterozoic environments.

Introduction

Deposition of banded iron formations (BIF) remains enigmatic, despite many years of research. Ongoing debates concern mechanisms to precipitate Fe and Si, physical depositional processes, redox conditions in the atmosphere-ocean system, primary mineralogy and subsequent diagenesis (Beukes & Klein 1992; Krapez et al. 2003; Beukes & Gutzmer 2008; Bekker et al. 2010; Posth et al. 2013). Banded iron formations represent a unique combination of processes, common in Archean-Paleoproterozoic rocks, but rarely replicated later (Bekker et al. 2010). From this perspective, transitions to under- and overlying non-BIF lithologies are particularly interesting, because they shed light on how environments and processes changed to allow BIF deposition. Previous studies have linked BIF deposition with transgressive phases when Fe-rich hydrothermal plumes were able to invade deep shelves (Beukes & Klein 1992; Simonson & Hassler 1996; Schröder et al. 2011). Major transgression was responsible for drowning of the Archean Campbellrand carbonate platform in South Africa, which is overlain by major Archean-Paleoproterozoic BIF (Beukes 1983; Beukes 1987).

On the other hand, the end of BIF deposition has received relatively little attention. There are few documented examples, namely the Hamersley Group in Australia (Morris & Horwitz 1983) and the Hotazel-Mooidraai formations in South Africa (Tsikos et al. 2001; Schneiderhan et al. 2006; Kunzmann et al. 2014). The Tongwane Formation in South Africa conformably overlies Archean-Paleoproterozoic BIF and was deposited on the eve of the Great Oxidation Event (GOE, ~ 2.42-2.32 Ga) (Martini 1979; Swart 1999). As such it can shed light on depositional and environmental conditions just prior to oxidation of the ocean-atmosphere system, and how they were linked to termination of BIF deposition. Deposition may have ended because oxidative weathering provided sufficient sulphate so that Fe was preferentially buried as pyrite (Canfield 2005). Alternatively, the Fe supply was effectively exhausted, either by precipitation itself, or because the hydrothermal Fe source was shut off (Holland 2006), possibly linked to global tectonics (Barley et al. 2005). Changes in relative sea level constitute a control external to the Fe precipitating system. As the Tongwane Formation includes deep- and shallow-water deposits, processes spanning a range of paleo-bathymetries can be potentially observed.

Based on detailed sedimentological field observations and bulk-rock geochemical analyses, this study builds the sedimentological framework of the Tongwane Formation. Depositional processes are identified, and their implications for termination of BIF deposition are discussed.

Geological Setting

The Tongwane Formation represents a thin dolomite unit that conformably overlies Paleoproterozoic BIF. It is only recorded from the Transvaal sub-basin in northeastern South Africa, where it forms a thin and poorly exposed outcrop belt around the northeastern Bushveld intrusion (Fig. 1) (Martini 1979). In this area, the unit conformably overlies the Penge Iron Formation (Chuniespoort Group of the Transvaal Supergroup) (Fig. 2). The BIF have been metamorphosed to amphibolite grade (~550°C in study area) in the Bushveld intrusion aureole (Miyano & Beukes 1997). Overlying strata have been assigned to the Duitschland and Timeball Hill formations (Pretoria Group), and the Tongwane Formation is only locally preserved beneath the base Duitschland erosional unconformity (Martini 1979).

No absolute age dates exist for the Tongwane Formation. An age of 2,480±6 Ma was obtained for the conformably underlying Penge Iron Formation (Nelson et al. 1999). Magmatic zircons in the Kuruman and Griquatown Iron Formations preserved in the Griqualand West sub-basin (equivalent to the Penge Iron Formation) have U-Pb ages between ~2,490-2,440 Ma (Pickard 2003; Beukes & Gutzmer 2008). Above the Tongwane Formation, the Timeball Hill Formation was dated at 2,316±7 Ma (Hannah et al. 2004) and 2,310±9 Ma (Rasmussen et al. 2013), whereas detrital zircons from the Duitschland Formation yielded a maximum depositional age of 2,424 Ma (Dorland 2004). However, unconformities occur between these three formations (Dorland 2004), and the Tongwane Formation must be significantly older.

Methods

The Tongwane Formation was studied in its type locality in Tongwane Gorge (24°10'44"S, 29°55'52"E). Outcrops were mapped (Fig. 3), followed by logging of a detailed stratigraphic section (Fig. 4), and sampling. Facies and petrographic analysis, including point counting (n=300), reflected light and cathodoluminescence microscopy were carried out on 22 hand samples and thin sections.

X-Ray Diffraction (XRD) and X-Ray Fluorescence (XRF) analysis were conducted at the Williamson Research Centre, University of Manchester to determine mineralogical and elemental composition, respectively. Mineralogy was determined using a Bruker D8 Advance Diffractometer (Cu Kα X-ray source); samples were scanned from 5 to 70° 2θ using a step size of 0.02° and a counting time of 0.2 seconds per step. Results are shown in Table 1 and Figure 4.

Pellets for XRF analysis were prepared by mixing 12 g of milled sample with 3 g of Hoechst wax carbon at 350rpm for 6 minutes in an agate mill. The mixed sample is then is placed in a 40 mm pellet die and pressed to 6 tons. The resultant pellet was analyzed using an Axios Sequential X-Ray Fluorescence Spectrometer. Accuracy, precision and limits of detection (LOD) were determined from known standards. Major element analysis accuracy was better than ± 0.52% and precision was better than 0.54%. Limits of detection were calculated for each element, and any data failing to exceed the LOD were omitted. Major element data are shown in table 2 and figures 5 and 6.

Facies analysis

Stratigraphic overview

Banded iron formation gradually passes via shales and siliceous mudstones (including a nodular cherty and Fe-rich horizon, about 20m thick), to dolomites (Martini 1979). This study placed the top of the Penge Iron Formation at the last major outcrop of iron formation (20m in Fig. 4). This is stratigraphically lower than Swart (1999) and adds a significant thickness of mudstone to the Tongwane Formation. The dolomites are overlain at 240m with a sharp contact by shales and occasional thin quartzites (Figs. 3, 4). Previous studies have taken this as the unconformable contact between the Tongwane and Duitschland formations, based on the presence of a chert breccia (Martini 1979; Swart 1999). This study did not identify such a breccia, but a local dip change of 20° could indicate an angular unconformity (Fig. 3). A diamictite bed 60m above this contact provides evidence that overlying strata likely belong to the Duitschland Formation (Figs. 3, 4). Intervening strata contain thin stromatolitic dolomite beds, which could belong to either the Tongwane or Duitschland Formation. Here the top of the thick dolomite unit at 240m is taken as the top of the Tongwane Formation, in accordance with previous workers. Consequently, the Tongwane Formation is 220m thick according to this study and dolomites make up only a small fraction of its total thickness.

Facies

Banded iron formation (Table 3)

Banded iron formation displays regular interbedding of Fe oxides, chert and siderite at a bed and lamina scale (Fig. 7A). Centimetric nodules of siderite/sideritic chert occur locally.

Riebeckite commonly replaces Fe-oxide rich layers. Iron formation samples have high Fe_2O_3 and SiO_2 concentrations (Fig. 5A), high Fe/Ti ratios and low Al/(Al+Fe+Mn) ratios (Fig. 6B).

The regular bedding, fine-grained nature of chemical sediments, and absence of traction sedimentary structures suggest a deeper-water environment below storm-wave base. The predominance of Fe over Al in samples suggests a hydrothermal source, consistent with existing models for the Penge IF (Beukes 1983; Miyano & Beukes 1997).

Shale (Table 3)

Shales follow with a gradual contact on the iron formation. Shales are moderately hard and consist of regular thin beds that weather in a characteristic blocky-tabular nature (Fig. 7B). Strata locally contain cm-thick interbeds and nodules of ferruginous dolomite and chert.

Similar to BIF, shales were deposited in deeper-water below storm-wave base, as evidenced by the largely regular bedding pattern, fine grain size, and absence of any sedimentary structures related to traction currents.

Siliceous mudstone and shale (Table 3)

From 88m upwards, rocks take on a more irregular-nodular weathering aspect, and they tend to be harder, probably as a result of stronger silicification (Fig. 8A). More siliceous beds are interstratified with softer shale horizons and locally with nodules and beds of ferruginous dolomite (Fig. 8B). Thin sections show abundant fine-grained angular detrital quartz, clay minerals and biotite, which locally form distinct mm-scale sandstone laminae (see below; Fig. 8C). Grunerite locally obscures any primary depositional microtextures (e.g. between 88-110m). Between 88-110m these rocks locally preserve mm-scale alternations of chert, Fe-oxides, riebeckite, and ankerite, reminiscent of the underlying BIF.

The more nodular siliceous mudstones represent a depositional environment probably very similar to underlying facies. Diagenetic silica formation was likely responsible for the more nodular aspect compared to underlying facies. The fine-grained detrital material reflects elevated detrital input. Interbedded sandstones are interpreted as gravity deposits (see below), and consequently suggest presence of a slope. Chert-Fe-oxide-riebeckite laminae reflect episodic re-appearance of BIF depositional processes, possibly in competition with clastic input. Biotite represents metamorphic recrystallization of sedimentary clays, whereas grunerite derives from original Fe-minerals in the interbedded BIF horizons.

Siliceous mudstone and shale with dolomite interbeds and nodules (Table 3)

From about 188m the amount of dolomite increases, and shales/siliceous mudstones are thinly interbedded with beds and nodules of dolomite (Fig. 8E). Dolomite interbeds can represent up to 50% of thickness in individual sections. Dolomite beds are largely free of clay minerals and biotite, and locally show flat and wavy lamination. Slump structures up to 1-2m in scale are common in this unit (Fig. 8D).

The depositional environment was similar to that of shale and siliceous mudstone, but increasing frequency of dolomite interbeds suggests export of carbonate from a shallow-water platform area and/or in-situ carbonate precipitation. Slumps indicate episodic sediment movement on a slope.

Dolomite with mudstone seams (Table 3)

This facies represents a 2m-thick transition zone between the mudstone-dominated facies below and the massive dolomite above. The lower contact is gradual. About 60% of its thickness is made up from cm- and dm-thick dolomite beds (Fig. 8F), which are laterally more persistent than stratigraphically lower dolomite. Domal structures, possibly stromatolites and/or slumps, occur (Fig. 8F). Siliceous mudstone beds form 2 prominent beds near the top of this unit.

Mudstone was deposited in a generally quiet environment (possibly below storm-wave base). Carbonate could reflect periods of in-situ carbonate formation and/or increasing export of shallow-water carbonate sediment. Stromatolite structures indicate at least episodic benthic carbonate accumulation, but since their biological composition is unknown, they do not constrain paleo-bathymetry. Possible slump structures suggest a slope setting.

Massive dolomite (Table 3)

With a sharp and slightly irregular contact, massive dolomite overlies the transitional dolomite (Fig. 9A). The facies is thick bedded with undulating bed contacts, and has local shale seams (Fig. 9B). Flat to wavy lamination occurs throughout (Fig. 9B); despite the generally poor preservation, some of it may in fact represent wave ripples. Hummocky cross-stratification was found in one place near the top of the unit. A bedding surface 7m below the top exposes symmetrical wave ripples (Fig. 9C). Ripple crests have paleo-azimuths between 120° and 130°. Lamination becomes more crinkly near the top and locally forms cm-scale domal stromatolites that are commonly traced by chert nodules (Fig. 9D). Stylolites are preserved in some samples and are often overprinted by euhedral pyrite crystals. Bulk samples contain 3-11wt.% Fe_2O_3 and 4-10wt.% SiO_2.

The rather clean carbonate with little detrital material and the preserved sedimentary structures indicate deposition in relatively shallow water away from clastic input. Lower parts of the dolomite were deposited at least above storm-wave base, while the upper parts represent deposition in shallow water above fair weather wave base. Much of the wavy lamination in the lower part could actually represent wave ripples, despite their poor preservation. Where well preserved, wave ripples indicate a paleo-shoreline trending NW-SE, consistent with paleogeographic reconstructions for the overlying Duitschland Formation (Coetzee 2001). The development of sedimentary structures related to traction and oscillatory flow suggests at least silt-grade grain size, although no trace of original grains has been preserved by dolomitization.

Sandstones and conglomerates (Table 3)

At various stratigraphic levels, sandstones and conglomerates are interbedded with the siliceous mudstones and dolomites (Fig. 4). Individual sandstone beds are 2-3mm thick. They consist of planar laminated fine-grained sandstones fining upwards through silt grade and terminating in mud/clay horizons (Fig. 8C).

A single chert conglomerate, a few cm thick, occurs at 188m (Fig. 4). The conglomerate contains granule to fine pebbles of chert. The margins of these clasts have been extensively overprinted by grunerite and magnetite-hematite.

The graded fine sandstones are interpreted as the uppermost portions (D and E horizons) of a Bouma sequence (Bouma 1962), i.e. as very distal portions of a turbidite flow with little erosive power. The conglomerate could be related to the slump structures observed, and may represent a coarse turbidite or a fine debris flow. Together, these features indicate episodic gravity-driven transport processes on a slope.

Evidence for platform margin collapse in the Tongwane Formation

A 50m high outcrop of Tongwane Formation was mapped in particular detail (Fig. 3), complemented by a stratigraphic log at the eastern end of the outcrop (Fig. 4). The center of the cliff was not accessible, and no sedimentological data have been collected.

Observations

A dolerite dyke, striking NW-SE, cuts across Tongwane stratigraphy at the eastern end of the outcrop. Tongwane siliceous mudstones with dolomite interbeds and nodules are exposed around much of the base of the outcrop. Along the logged section, they pass gradually to dolomite with mudstone interbeds (210m on log), which in turn are sharply overlain (212m on log) by the massive Tongwane dolomite that makes up the bulk of the cliff. Near the top of the cliff (240m on log), the dolomite passes with a sharp contact to shales and quartzites; these have been assigned to the Duitschland Formation, although no absolute age constraints exist (Martini 1979; Swart 1999). Further westward, the contact occurs at the top of the outcrop, apparently climbing through the stratigraphy. This seemingly erosive nature of the contact cannot be verified, as the center of the cliff is of difficult access. In the log, no change in strike and dip occurs at the contact, but a gentle difference in dip (20°) was observed at the top of the cliff.

A breccia occurs at the center base of the outcrop. Interbedded shales and dolomites display a progressive increase in brecciation from the west towards the center of the outcrop; the following zones can be distinguished (Figs. 3, 10):

Zone 1: Thin bedded stratification with preserved interbedding (Fig. 10A). The mudstones stand out as a result of silicification. Dolomites are massive and laminated. Locally, closed fractures cut through the mudstones, but do not affect the dolomite. Rare bigger fractures affect several strata but die out vertically over 1-2m. Larger fractures are filled by massive dolomite and mudstone clasts up to a few cm in diameter (Fig. 10A).

Zone 2: The interbedding is preserved, but regularly spaced fractures, filled with dolomite, separate the mudstone beds into individual blocks (Fig. 10B). These blocks appear like tablets that can still be fitted together. The gaps occur on cm-dm scale. Going eastward, some smaller and flat clasts start to be rotated.

Zone 3: With a sharp boundary, the coherent tablets of zone 2 pass to a massive breccia (Fig. 10C). Some clasts are rotated somewhat from the horizontal, but most show a chaotic, clast-supported fabric. Clast size varies from few mm to 40cm. Massive dolomite forms the matrix. The contact between zones 2 and 3 is inclined at an angle of 30-40°; further east it turns almost horizontal and follows the base of the cliff (Fig. 3). Breccia zone 3 is about 4-5m thick.

Zone 4: The breccia laterally and vertically passes to massive dolomite with a gradual contact (Fig. 10D). Inspection from the outcrop base suggests the massive dolomite occupies the basal 10m of the cliff. The massive dolomite is about 20m wide. It locally contains streaks of mudstone facies.

Zone 5: At its eastern contact, the massive dolomite interfingers with interbedded mudstone and dolomite facies. Compared to zone 1, the interbedding is on a finer scale (less than 4cm), and is dominated by mudstone facies. Several m-scale slump features have been observed (Fig. 8D).

The interbedded facies of zone 5 can be traced laterally to the same facies in the measured log (about 200-210m on log, Fig. 4). The eastward continuation of zones 3 and 4 is covered by vegetation. The massive Tongwane dolomite can be seen overlying mudstone and dolomite westwards from the log; it is inferred to sit atop the massive dolomite of zone 4 in the center of the cliff based on very similar weathering. This cannot be confirmed due to the inaccessibility of the central cliff face.

Interpretation

The gradual lateral change from well-bedded lithologies to a chaotic breccia indicates progressive displacement of the original lithology. Initially, boudins are formed (Ramberg 1955), followed by clast rotation. Boudinage is characteristic of deformation in lithologies with competency contrasts (Ramberg 1955). In this case, the silicified mudstones acted as brittle layers, whereas the dolomite (or its precursor) had a more ductile behavior. The increase in strain from zone 1 to 5 corresponds to horizontal extensional forces.

While boudinage is common in metamorphic terrains, it has equally been reported from a number of sedimentary cases. Most prominent are ‘chocolate tablets’ of relatively more competent carbonate beds in ductile deformed sulfate evaporites (Lugli 2001). Chert-carbonate and intra-carbonate competency contrasts and boudinage have been reported as well (Kolodny 1969; Lu et al. 2006). On a larger scale, Alonso et al. (2008) have described gravitational collapse of a passive margin, where some of the deformation is represented by sandstone and limestone boudins in shale. Extension in a sedimentary or tectonic environment is the common driving force for boudinage and deformation (Lugli 2001; Lu et al. 2006), but sedimentary overburden and diagenetic redistribution of silica, creating the competency difference, may have a similar effect (Kolodny 1969).

A purely tectonic origin for the observed breccia, due to successive movement along an extensional fault, is unlikely in the present case. The breccia only occurs on the western side of the outcrop. Strata do not show obvious displacement between the western and eastern portions of the outcrop, and there is no evidence for faulting at the top of the outcrop. The change in dip of the brecciated zone further argues against post-depositional faulting, and makes a sedimentary origin more likely. The stratigraphic position between deeper-water iron formations and shallow-water carbonates, and the lateral passage to slump structures favor tectonic or gravitational collapse of a platform slope. This would have created the tensional forces that caused progressive lateral deformation of slope deposits. The end result was a debris flow breccia. This process further requires that mudstones were primarily siliceous or at least were silicified very quickly to behave in a brittle manner.

Depositional model for BIF-Tongwane transition

The gradual transitions between facies, and the progressive increase in energy level through the stratigraphic section suggest an overall shallowing succession, which terminates with wave-swept shallow-water platform carbonates (Fig. 11). It is unknown whether preserved microbial structures reflect photosynthetic organism and thus formed in the photic zone. The association with shallow-water oscillatory flow however suggests water depth did not exceed a few 10's of meters. Deposition of BIF occurred on the deep shelf, likely at 100-200m water depth or more (Simonson & Hassler 1996; Beukes 2004)

Slope depositional processes repeatedly occurred in the sedimentary transition, as demonstrated by thin turbidites, slumps and slope collapse brecciation (Fig. 11-2). The progressive increase in carbonate beds through the succession, and in particular between 190-214m reflects increased export of carbonate mud produced photosynthetically on a platform top

(Schneiderhan et al. 2006), in-situ formation of carbonate within or below the photic zone, early diagenetic carbonate formation (Beukes & Gutzmer 2008; Fischer et al. 2009), or a combination of these (Fig. 11-3). Benthic stromatolites below the massive carbonate suggest that at least in the final stages of transition, carbonate was forming in-situ on the upper slope. The carbonate platform, where at least some of this carbonate originated, subsequently prograded over the slope deposits (Fig. 11-3). Although the gradual shallowing would suggest ramp geometry, wave-cross bedded dolomites could reflect a platform-margin shoal. In addition, slope collapse indicates significant relief at the margin and a break in the platform depositional profile (Fig. 11-3).

The depositional change from BIF to shale clearly reflects an increase in fine clastic detritus into depositional environments (Fig. 11-2), which is also documented by increasing Al concentrations (Fig. 5D). It is unclear whether proximal carbonate depositional environments existed at this time in areas unaffected by siliciclastics (Fig. 11-2). There is little evidence to suggest significant shallowing at the base of the Tongwane Formation, and true slope deposits appear only 70-80m higher in the stratigraphy. However, siliciclastic input predates export of shallow-water carbonate (Fig. 11-2).

More nodular siliceous mudstones at around 88-110m locally contain alternations of chert, Fe-oxides, riebeckite, and ankerite. However, depositional textures are strongly overprinted by metamorphic minerals, in particular grunerite. The overprint does not allow a full depositional assessment of this section, but BIF deposition may have resumed episodically (Fig. 11-2), underlining the transitional nature of the basal Tongwane Formation.

In summary, the Tongwane succession records shallowing from deep shelf (BIF) through slope deposition with distal turbidites, to shallow-water carbonates with wave ripples and stromatolites (Fig. 11). Carbonates were deposited on a platform with a distally steepened ramp profile.

Discussion

The transition from BIF to Tongwane platform carbonates is conformable, similar to other documented BIF-to-carbonate transitions (Simonson et al. 1993). In coeval strata in Australia, the transition from the Marra Mamba IF to the deeper-water Wittenoom dolomite contains carbonate debris flow deposits that derived from a fairly steep platform margin (Morris & Horwitz 1983; Simonson et al. 1993). The equivalent shallow-water facies are represented by the Carawine dolomite (Simonson et al. 1993). At the same time, Fe and chert deposition repeatedly alternated with carbonate and subordinate silica deposition until the latter dominated (Morris & Horwitz 1983). The other well-documented BIF-to-carbonate transition occurs in the ~2.3-2.2 Ga old Hotazel IF to Mooidraai Formation in South Africa (Schneiderhan et al. 2006; Kunzmann et al. 2014). Again, the passage from deeper-water iron and manganese formations to shallow-water carbonates is gradual, with progressive increase in $\delta^{13}C$ due to dominance of inorganic carbon in the carbon isotope pool (Schneiderhan et al. 2006; Kunzmann et al. 2014).

The Tongwane section provides a unique opportunity to observe the transition from Archean-Paleoproterozoic BIF to non-BIF deposition and the drivers for this change. This has potential implications for understanding controls on oxygen build-up in the subsequent GOE. Two scenarios are possible:

1) As BIF commonly pass up-section to shallow-water facies, it may be deduced that regression caused shallowing of the environment, thus the inverse to the transgressive scenario invoked commonly for the initiation of BIF deposition. A variant to this scenario is dilution of Fe by input of other sediment sources (carbonate or siliciclastic). Such external factors may have pushed BIF deposition to central parts of the basin, while other lithologies, such as carbonate platforms, dominated around the basin margins. Increase in detrital sediment input and/or a sedimentary record of shallowing are evidence for this scenario. Hydrothermal Fe supply may be masked to a variable degree.

2) Factors intrinsically linked to the Fe depositional system changed so as to stop or at least restrict BIF deposition irrespective of external controls. Such intrinsic factors include retreat and possibly complete disappearance of the hydrothermal plume delivering Fe to the depositional site, but equally a change in oceanic redox conditions affecting BIF depositional processes. On the other hand, increased hydrothermal activity and plume expansion could restart BIF deposition. A hydrothermal signature for Fe should disappear completely in such a scenario.

Recognizing relative roles of intrinsic and external factors in the present case relies on careful examination of the sedimentary and geochemical records. This analysis remains ambiguous however, given the metamorphic overprint of the Tongwane Formation, but equally because such processes seldom operate independently.

Sedimentological evidence from the entire succession suggests an overall shallowing trend, but shallowing at the BIF-Tongwane contact itself is ambiguous due to the absence of bathymetry indicators. Observations indicate increased detrital input above the Penge IF. The sedimentological transition at about 20m to non-BIF facies occurs over a fairly short vertical distance, recognizable by different weathering and an increase in Al_2O_3 (see below). Turbidites in siliceous mudstones higher up demonstrate detrital input and slope deposition, which is absent from the underlying BIF. As discussed before, the progressive increase in carbonate interbeds and nodules reflects at least partly export of carbonate mud produced photosynthetically on a platform top.

Major elements show systematic changes of increasing CaO, MgO, and Al_2O_3 from BIF to carbonates. However, the increase in CaO effectively only starts about 10m below the massive carbonate unit, possibly reflecting increased carbonate export (see above) (Schneiderhan et al. 2006). Metamorphic overprint of the Tongwane Formation through biotite formation means that metamorphic processes could have affected MgO and Al_2O_3 trends. Aluminium is however correlated with TiO_2 (Fig. 6A). As both Al and Ti are linked to continental weathering (Taylor & McLennan 1985), there is independent evidence that Al_2O_3 can be used as a monitor for detrital input in the Tongwane Formation. Most likely, any metamorphic remobilization of Al occurred between detrital clay minerals and biotite forming from them, thus not involving major spatial redistribution of Al. On this basis, detrital input indeed increased above the BIF units, which is further reflected in thin quartzose turbidites (see above).

Neither Fe_2O_3 nor SiO_2 display any systematic upsection changes between Penge BIF and Tongwane carbonate. To some extent, this trend likely reflects effective Fe and Si remobilization through metamorphic neoformation of riebeckite and grunerite. Although Fe remobilization has occurred, observations suggest dominant depositional control over current Fe_2O_3 concentrations. Enrichment of Fe over Al decreases upsection (Fig. 5B). When Fe is normalized to Ti and compared to Al, samples show a mixing between Fe-rich and Al-rich end members (Fig. 6B). Poles reflect equivalents of modern hydrothermal muds and continental detrital input, respectively (Boström & Peterson 1969; Taylor & McLennan 1985; Chester 2000). Signatures of hydrothermal Fe occur as high as 203m in the section. A well-defined mixing trend between hydrothermal and detrital poles, and persistent hydrothermal signatures until below the Tongwane dolomite strongly suggest masking of hydrothermal input by detrital input, rather than reduced venting of hydrothermal plumes.

Hydrothermal venting and chemocline transgression may explain the re-appearance of BIF facies at 88-110m and demonstrate that the transition BIF-carbonate was not a unidirectional process. It remains unclear whether these BIF facies reflect variations in venting of the hydrothermal Fe source (chemocline transgression), small transgressive pulses (with static chemocline), or a combination, as venting could be linked to relative sea level rise via increased activity at mid-ocean ridges. Presence of thin turbidite beds clearly indicates that BIF deposition was partly countered by detrital input.

In summary, decoupling external and intrinsic factors in the BIF-carbonate transition remains difficult, and both may have contributed to the end of BIF deposition and establishment of carbonate platforms. There is however a distinct line of evidence that increased detrital input coupled with the overall shallowing of depositional environments effectively suppressed BIF deposition. A weakened hydrothermal signal seemingly persisted throughout deposition of Tongwane shales and siliceous mudstones. At the same time, BIF deposition episodically resumed as a consequence of transgression, increased hydrothermal venting, or both.

The trends discussed above suggest that establishment of the Tongwane carbonate platform was coeval with restriction of BIF deposition to deeper parts of the basin, which are not preserved any more (Fig. 11-3). The presence of minor but distinct detrital input stratigraphically between BIF and carbonates raises the question of source for these clastics. As has been postulated for the Griqualand West sub-basin, end of BIF deposition may have roughly coincided with uplift across the Kaapvaal Craton and renewed clastic input (Schröder et al. 2011).

Based on this study, the end of BIF deposition in the earliest Paleoproterozoic has at least as much to do with external factors such as relative sea level and dilution of Fe sources by detrital sediment input, as with intrinsic factors such as Fe supply and redox changes. Consequently, this reduces the implications of the end of Archean-Paleoproterozoic BIF deposition for our understanding of geochemical processes operating in the buildup to the GOE.

Conclusion

This study has investigated the sedimentology and bulk-rock geochemistry of the Tongwane Formation. The Tongwane Formation records the end of BIF deposition in the earliest Paleoproterozoic, and its transition to shallow-water platform carbonates. The following main conclusions can be drawn from the present study:

(1) The Tongwane Formation is 220m thick and conformable with the underlying Penge IF. A poorly developed unconformity separates it from overlying Duitschland Formation strata. The Tongwane contains from the base up shales, siliceous mudstones with local BIF facies, interbedded mudstones and dolomites, and a massive dolomite unit at the top. This succession

records shallowing from deep shelf (BIF) through slope deposition with distal turbidites, to shallow platform carbonates with wave ripples and stromatolites.

(2) The platform margin apparently had some relief, which is demonstrated by development of a carbonate debris flow breccia demonstrates platform margin collapse and some relief of the platform margin. Extensional forces created progressive deformation of the upper slope sediments, from slumping and fracturing through sedimentary boudinage, to brecciation. Sedimentary boudinage records a competency contrast between dolomites (ductile deformation) and siliceous mudstones, where early lithification (by silicification) caused a brittle behavior. Slumps are associated.

(3) Despite metamorphic overprint, bulk-rock Al and Fe concentrations still reflect at least partly sedimentary conditions. Aluminium traces detrital input together with titanium, and increases from BIF to carbonates. Iron concentrations remain fairly high throughout the Tongwane Formation, which partly reflects metamorphic remobilization of Fe-rich phases. On the other hand, Fe/Ti vs Fe/(Al+Fe+Mn) ratios of all samples plot on a mixing curve between hydrothermal (equivalent to modern hydrothermal muds) and detrital end members.

(4) Sedimentology indicates increase in detrital input from the end of BIF deposition. While the overall shallowing trend reflects regression, it is unclear whether it already set in at the top of BIF. The role of relative sea level in controlling BIF deposition, while clearly demonstrated in other cases, is ambiguous for the Tongwane Formation. Geochemistry suggests that a hydrothermal Fe signal persisted until below the Tongwane carbonate platform, and that detrital input progressive masked a hydrothermal plume.

(5) Although a partial or complete shutdown of the Fe source cannot be excluded, the weight of the evidence from the Tongwane Formation favors external factors such as relative sea level fall and Fe dilution by increased detrital input as the main drivers for the BIF-carbonate transition.

Acknowledgements

The authors wish to thank Jens Gutzmer for help in the field, and for providing the photo used in figure 3. Alastair Bewsher and Paul Lythgoe provided assistance with analytical work. Stefan Schröder acknowledges financial support for fieldwork through strategy grants of the Faculty of Physical Sciences and Engineering, and the School of Earth, Atmospheric and Environmental Sciences at the University of Manchester.

References

Alonso, J. L., Gallastegui, J., García-Sansegundo, J., Farias, P., Rodríguez Fernández, L. R. & Ramos, V. A. 2008. Extensional tectonics and gravitational collapse in an Ordovician passive margin: The Western Argentine Precordillera. *Gondwana Research*, **13**, 204-215.

Barley, M. E., Bekker, A. & Krapez, B. 2005. Late Archean to Early Paleoproterozoic global tectonics, environmental change and the rise of atmospheric oxygen. *Earth and Planetary Science Letters*, **238**, 156-171.

Bekker, A., Slack, J. F., Planavsky, N., Krapez, B., Hofmann, A., Konhauser, K. O. & Rouxel, O. J. 2010. Iron Formation: The sedimentary product of a complex interplay among mantle, tectonic, oceanic, and biospheric processes. *Economic Geology*, **105**, 467-508.

Beukes, N. J. 1983. Palaeoenvironmental setting of iron-formations in the depositional basin of the Transvaal Supergroup, South Africa. In: Trendall, A. F. & Morris, R. C. (eds.) *Iron formation: facts and problems*. Developments in Precambrian Geology, **6**, Elsevier, 131-209.

— 1987. Facies relations, depositional environments and diagenesis in a major Early Proterozoic stromatolitic carbonate platform to basin sequence, Campbellrand Subgroup, Transvaal Supergroup, Southern Africa. *Sedimentary Geology*, **54**, 1-46.

Beukes, N. J. & Klein, C. 1992. Models for iron-formation deposition. In: Schopf, J. W. & Klein, C. (eds.) *The Proterozoic biosphere*, Cambridge University Press, 147-151.

Beukes, N. J. 2004. Early options in photosynthesis. *Nature*, **431**, 522-523.

Beukes, N. J. & Gutzmer, J. 2008. Origin and paleoenvironmental significance of major iron formations at the Archean-Paleoproterozoic boundary. *Society of Economic Geologists Reviews*, **15**, 5-47.

Boström, K. & Peterson, M. N. A. 1969. The origin of Al-poor ferromanganoan sediments in areas of high heat flow on the East Pacific Rise. *Marine Geology*, **7**, 427-447.

Bouma, A. H. 1962. *Sedimentology of some flysch deposits: a graphic approach to facies interpretation*. Elsevier, 168.

Canfield, D. E. 2005. The early history of atmospheric oxygen: Homage to Robert M. Garrels. *Annual Reviews of Earth and Planetary Sciences*, **33**, 1-36.

Chester, R. 2000. *Marine geochemistry*. Blackwell.

Coetzee, L. L. 2001. *Genetic stratigraphy of the Paleoproterozoic Pretoria Group in the Western Transvaal*. MSc, Rand Afrikaans University, 212 pp.

Dorland, H. C. 2004. *Provenance ages and timing of sedimentation of selected Neoarchean and Paleoproterozoic successions on the Kaapvaal Craton*. Ph.D. Thesis, Rand Afrikaans University, 326 pp.

Fischer, W. W., Schröder, S., Lacassie, J. P. et al. 2009. Isotopic constraints on the Late Archean carbon cycle from the Transvaal Supergroup along the western margin of the Kaapvaal craton, South Africa. *Precambrian Research*, **169**, 15-27.

Hannah, J. L., Bekker, A., Stein, H. J., Markey, R. J. & Holland, H. D. 2004. Primitive Os and 2316 Ma age for marine shale: implications for Paleoproterozoic glacial events and the rise of atmospheric oxygen. *Earth and Planetary Science Letters*, **225**, 43-52.

Holland, H. D. 2006. The oxygenation of the atmosphere and oceans. *Philosophical Transactions of the Royal Society, London, series B*, **361**, 903-915.

Kolodny, Y. 1969. Petrology of siliceous rocks in the Mishash Formation (Negev, Israel). *Journal of Sedimentary Petrology*, **39**, 166-175.

Krapez, B., Barley, M. E. & Pickard, A. L. 2003. Hydrothermal and resedimented origins of the precursor sediments to banded iron formation: sedimentological evidence from the Early Palaeoproterozoic Brockman Supersequence of Western Australia. *Sedimentology*, **50**, 979-1011.

Kunzmann, M., Gutzmer, J., Beukes, N. J. & Halverson, G. P. 2014. Depositional environment and lithostratigraphy of the Paleoproterozoic Mooidraai Formation, Kalahari Manganese Field, South Africa. *South African Journal of Geology*, **117**, 173-192.

Lu, H., Zhang, Y., Zhang, Q. & Xiao, J. 2006. Earthquake-related tectonic deformation of soft-sediments and its constraints on basin tectonic evolution. *Acta Geologica Sinica*, **80**, 724-732.

Lugli, S. 2001. Timing of post-depositional events in the Burano Formation of the Secchia valley (Upper Triassic, Northern Apennines), clues from gypsum±anhydrite transitions and carbonate metasomatism. *Sedimentary Geology*, **140**, 107-122.

Martini, J. E. J. 1979. A copper-bearing bed in the Pretoria Group in northeastern Transvaal. In: Anderson, A. M. & van Biljon, W. J. (eds.) *Some sedimentary basins and associated ore deposits of South Africa*. Geological Society of South Africa Special Publication, **6**, Geological Society of South Africa, 65-72.

Miyano, T. & Beukes, N. J. 1997. Mineralogy and petrology of the contact-metamorphosed amphibole asbestos-bearing Penge Iron Formation, Eastern Transvaal, South Africa. *Journal of Petrology*, **38**, 651-676.

Morris, R. C. & Horwitz, R. C. 1983. The origin of the iron-formation-rich Hamersley Group of Western Australia — deposition on a platform. *Precambrian Research*, **21**, 273–297.

Nelson, D. R., Trendall, A. F. & Altermann, W. 1999. Chronological correlations between the Pilbara and Kaapvaal cratons. *Precambrian Research*, **97**, 165–189.

Pickard, A. L. 2003. SHRIMP U–Pb zircon ages for the Palaeoproterozoic Kuruman Iron Formation, Northern Cape Province, South Africa: evidence for simultaneous BIF deposition on Kaapvaal and Pilbara Cratons. *Precambrian Research*, **125**, 275-315.

Posth, N. R., Köhler, I., Swanner, E. D. et al. 2013. Simulating Precambrian banded iron formation diagenesis. *Chemical Geology*, **362**, 66-73.

Ramberg, H. 1955. Natural and experimental boudinage and pinch-and-swell structures. *Journal of Geology*, **63**, 512-526.

Rasmussen, B., Bekker, A. & Fletcher, I. R. 2013. Correlation of Paleoproterozoic glaciations based on U-Pb zircon ages for tuff beds in the Transvaal and Huronian Supergroups. *Earth and Planetary Science Letters*, **382**, 173-180.

Schneiderhan, E. A., Gutzmer, J., Strauss, H., Mezger, K. & Beukes, N. J. 2006. The chemostratigraphy of a Paleoproterozoic MnF-BIF succession - the Voelwater Subgroup of the Transvaal Supergroup in Griqualand West, South Africa. *South African Journal of Geology*, **109**, 63-80.

Schröder, S., Bedorf, D., Beukes, N. J. & Gutzmer, J. 2011. From BIF to red beds: Sedimentology and sequence stratigraphy of the Paleoproterozoic Koegas Subgroup (South Africa). *Sedimentary Geology*, **236**, 25-44.

Simonson, B. M., Schubel, K. A. & Hassler, S. W. 1993. Carbonate sedimentology of the early Precambrian Hamersley Group of Western Australia. *Precambrian Research*, **60**, 287-335.

Simonson, B. M. & Hassler, S. W. 1996. Was the deposition of large Precambrian iron formations linked to major marine transgressions? *Journal of Geology*, **104**, 665-676.

Swart, Q. D. 1999. *Carbonate rocks of the Paleoproterozoic Pretoria and Postmasburg Groups, Transvaal Supergroup*. MSc Thesis, Rand Afrikaans University, 126 pp.

Taylor, S. R. & McLennan, S. M. 1985. *The continental crust: its composition and evolution*. Blackwell, 312.

Tsikos, H., M., M. J. & Harris, C. 2001. Geochemistry of the Palaeoproterozoic Mooidraai Formation: Fe-rich limestone as end member of iron formation deposition, Kalahari Manganese Field, Transvaal Supergroup, South Africa. *Journal of African Earth Sciences*, **32**, 19-27.

Figure Captions

Figure 1: (A) Outcrops of the Chuniespoort and Pretoria Groups of the Transvaal Supergroup on the northeastern Kaapvaal Craton. (B) Detailed geological sketch of the study area (modified from Geological Map of the Republic of South Africa, Sheet 2428 Nylstroom, 1978).

Figure 2: Stratigraphy of the Chuniespoort and Pretoria Groups of the Transvaal Supergroup in the study area with relevant records of environmental oxidation.

Figure 3: General sketch of the outcrop for the main Tongwane dolomite, and the main stratigraphic relationships. Photo inset shows the basal inclined contact of the slope collapse breccia (for details of textures see figure 8).

Figure 4: Stratigraphic log (location see figure 3) of the Tongwane Formation with mineralogical information obtained by XRD analyses.

Figure 5: Stratigraphic trends of major elements: (A) Fe_2O_3; (B) Fe_2O_3 normalized to Al_2O_3; (C) SiO_2; (D) Al_2O_3; (E) CaO. For symbols of stratigraphic log see figure 2.

Figure 6: (A) Cross plot of Al_2O_3 vs. TiO_2 as independent monitors for detrital input. (B) Fe/Ti vs Al/(Al+Fe+Mn) cross plot that enables identification of a hydrothermal component. Reference points are the compositions of modern hydrothermal muds from the East Pacific Rise (Boström & Peterson 1969; Chester 2000) and Post-Archean Average Shale (PAAS) (Taylor & McLennan 1985).

Figure 7: Banded iron formation and shale facies. (A) Mesobanded BIF with Fe-oxide-rich (grey) and chert-rich laminae (brownish) (10m in figure 4). (B) Blocky weathering and more regular bedding characteristic of the shales (30m in figure 4; hammer for scale indicated by circle).

Figure 8: Siliceous mudstone facies. (A) Nodular aspect of siliceous mudstones above 88m (hammer for scale indicated by circle). (B) Thin ankerite lamina interbedded with siliceous mudstones (90m in figure 4). (C) Thin laminae of fine sand to silt-grade quartz grains (light colored) in carbonate. Weak fining-upward indicates deposition from a turbidity current (102m in figure 4). (D) Metric slump in siliceous mudstones at a stratigraphic level equivalent to 211m of

section. Location indicated in fig. 4. (E) Dolomite nodules and bands interbedded with siliceous mudstone (208m in figure 4). (F) Centimetric stromatolitic bed of dolomite in siliceous mudstones (211m in figure 4).

Figure 9: Carbonate facies. (A) The main Tongwane dolomite overlies siliceous mudstones with a sharp contact (at hammer) (213m in figure 4). (B) Wavy lamination of main dolomite, interpreted as wave ripples (223m in figure 4). (C) Wave ripples on bedding plane of main dolomite (233m in figure 4). (D) Silicified stromatolite head (237m in figure 4).

Figure 10: Photos representing successive stages of stratal collapse in the Tongwane Fm. (A) Zone 1: Bedding preserved, with fractures affecting siliceous mudstones. Larger fractures (at right) are filled with dolomite and mudstone clasts. (B) Zone 2: Formation of chocolate tablets by regularly spaced fractures or gaps filled with dolomite. (C) Zone 3: Sharp contact (arrowed) between largely intact bedding on the right and individualized clasts that have been rotated and are supported by dolomite groundmass. Left scale bar in cm. (D) Zone 4: Zone 4: Massive dolomite (top) overlies individual breccia clasts and undeformed mudstones at the bottom. Left scale bar in cm.

Figure 11: Depositional models showing the evolution of environments and depositional processes. The NE-SW paleodip of the shelf has been reconstructed using paleocurrent data from the Tongwane dolomite. Basin margin and basin center are hypothetical, as these areas are not preserved in current outcrops. (1): Deep shelf deposition of BIF. (2) Deposition of siliceous mudstones with detrital input. Iron formations are interbedded with mudstones, which could reflect sea level variations as well as hydrothermal venting. (3) Progradation of a distally steepened carbonate ramp over slope/outer ramp deposits.

Table 1: XRD data

Table 2: XRF data

Table 3: Summary of facies observations and interpretations.

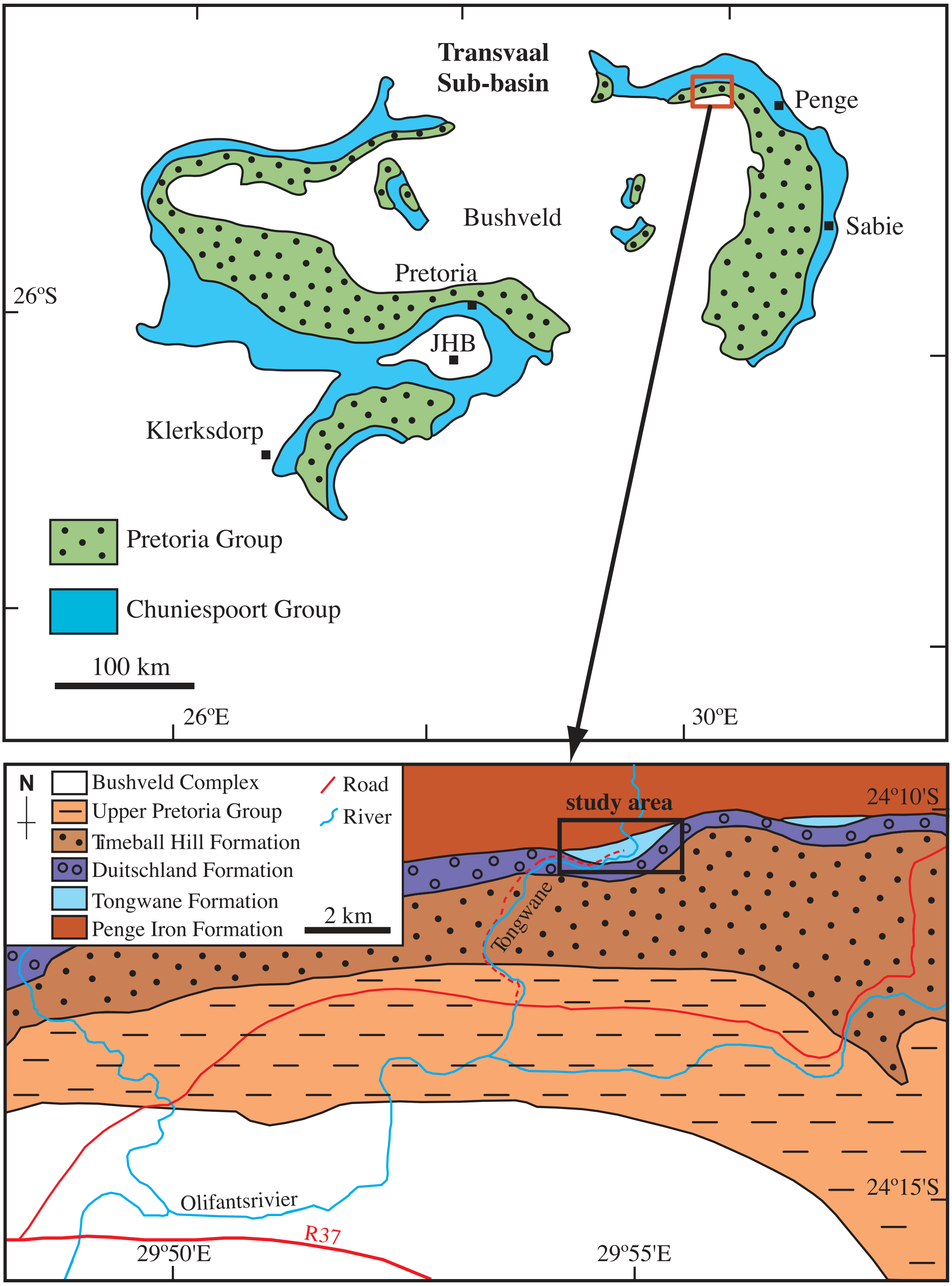
Transvaal Sub-basin
Penge
Bushveld
Sabie
Pretoria
26ºS
JHB
Klerksdorp
Pretoria Group
Chuniespoort Group
100 km
26ºE
30ºE
N
Bushveld Complex
Upper Pretoria Group
Timeball Hill Formation
Duitschland Formation
Tongwane Formation
Penge Iron Formation
Road
River
2 km
study area
24º10'S
Tongwane
Olifantsrivier
R37
29º50'E
29º55'E
24º15'S

Figure 1

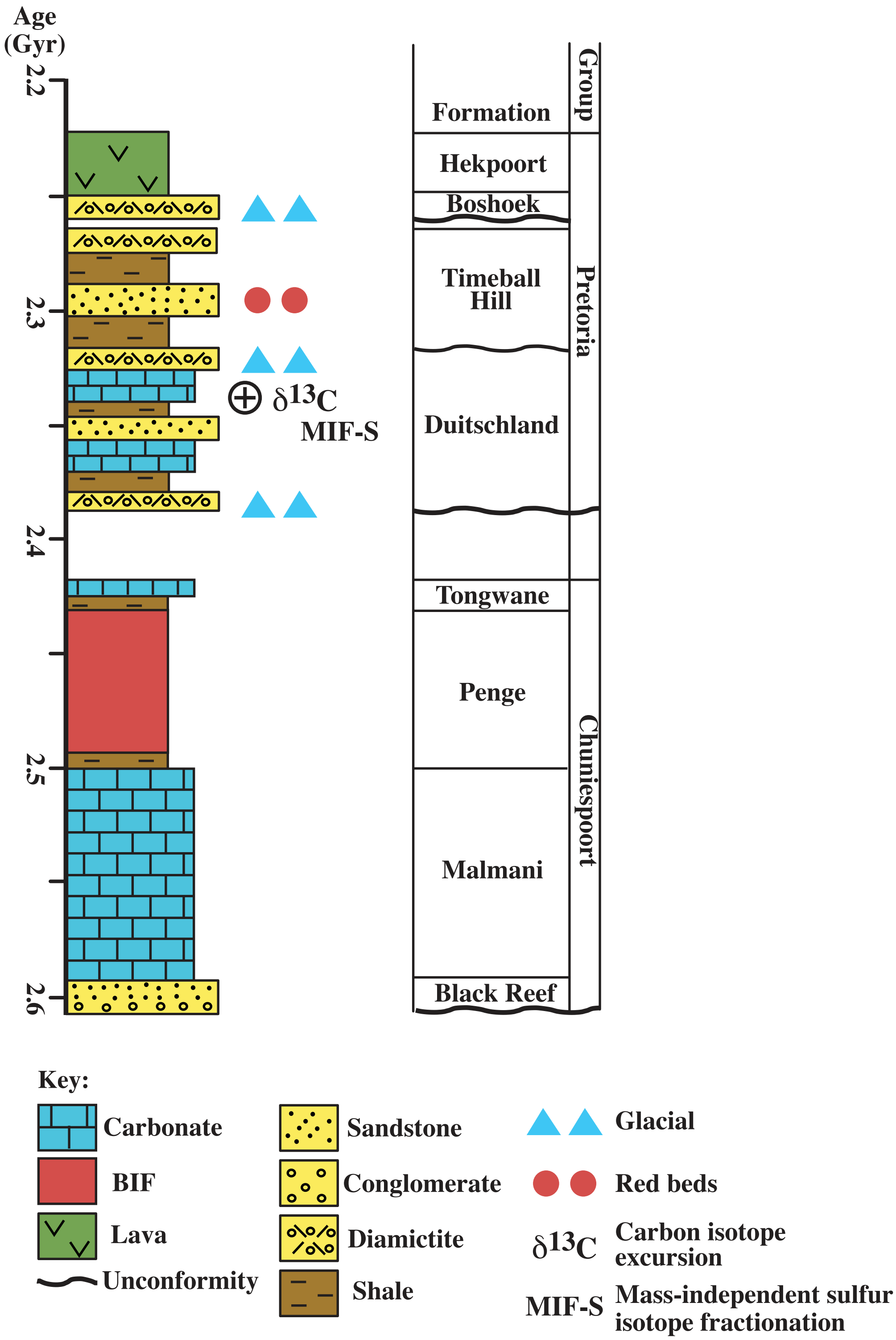

Age
(Gyr)
2.2
2.3
2.4
2.5
2.6
δ13C
MIF-S
Formation
Group
Hekpoort
Boshoek
Timeball Hill
Duitschland
Tongwane
Penge
Malmani
Black Reef
Pretoria
Chuniespoort
Key:
Carbonate
BIF
Lava
Unconformity
Sandstone
Conglomerate
Diamictite
Shale
Glacial
Red beds
δ13C Carbon isotope excursion
MIF-S Mass-independent sulfur isotope fractionation

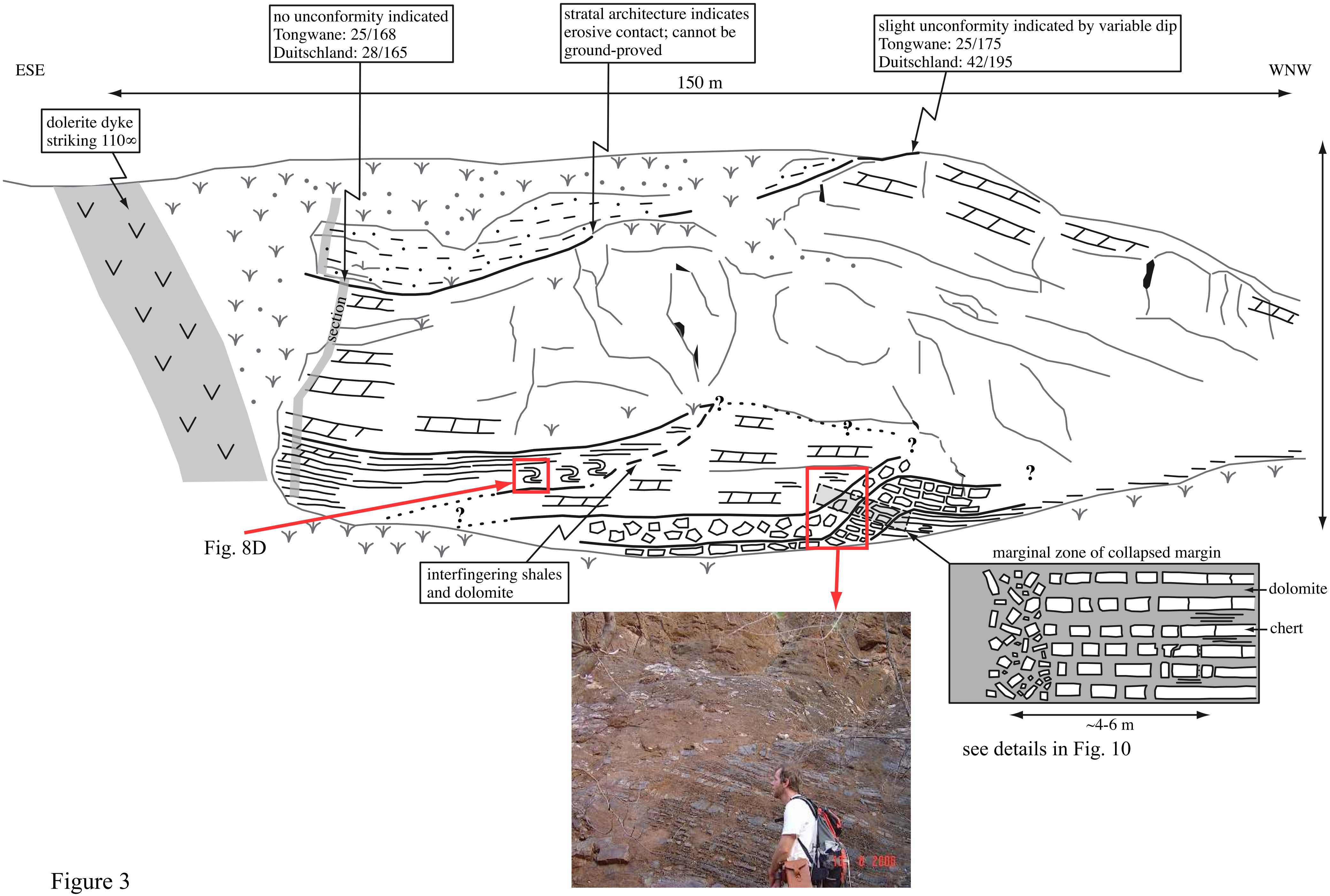
no unconformity indicated
Tongwane: 25/168
Duitschland: 28/165
stratal architecture indicates
erosive contact; cannot be
ground-proved
slight unconformity indicated by variable dip
Tongwane: 25/175
Duitschland: 42/195
ESE
WNW
150 m
dolerite dyke
striking 110∞
section
50 m
?
Fig. 8D
interfingering shales
and dolomite
marginal zone of collapsed margin
dolomite
chert
~4-6 m
see details in Fig. 10
12 8 2006

Figure 3

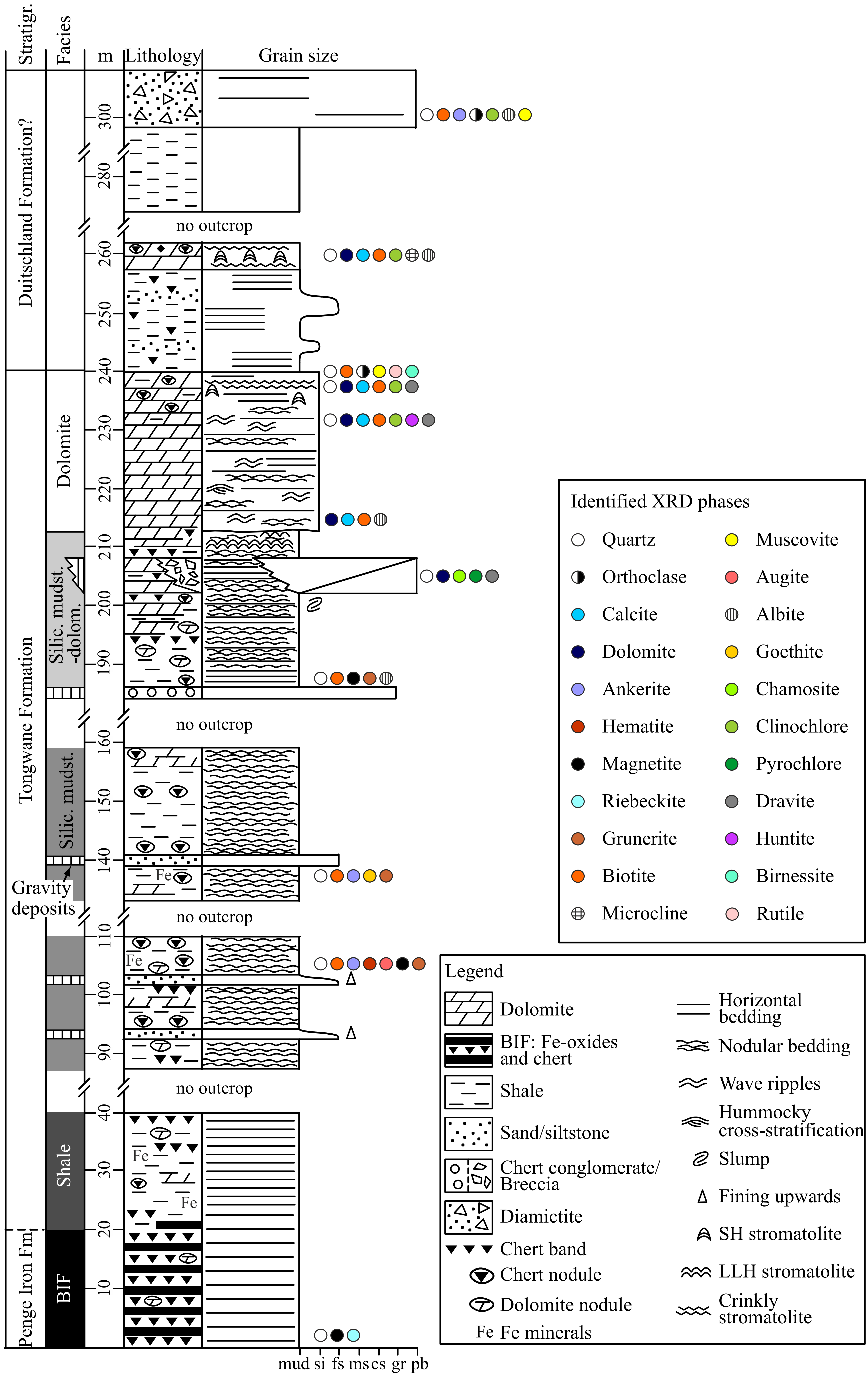

Stratigr.
Facies
m
Lithology
Grain size
Duitschland Formation?
Tongwane Formation
Penge Iron Fm
Dolomite
Silic. mudst. -dolom.
Silic. mudst.
Gravity deposits
Shale
BIF
no outcrop
Fe
mud si fs ms cs gr pb
Identified XRD phases
Quartz
Orthoclase
Calcite
Dolomite
Ankerite
Hematite
Magnetite
Riebeckite
Grunerite
Biotite
Microcline
Muscovite
Augite
Albite
Goethite
Chamosite
Clinochlore
Pyrochlore
Dravite
Huntite
Birnessite
Rutile
Legend
Dolomite
BIF: Fe-oxides and chert
Shale
Sand/siltstone
Chert conglomerate/ Breccia
Diamictite
Chert band
Chert nodule
Dolomite nodule
Fe Fe minerals
Horizontal bedding
Nodular bedding
Wave ripples
Hummocky cross-stratification
Slump
Fining upwards
SH stromatolite
LLH stromatolite
Crinkly stromatolite

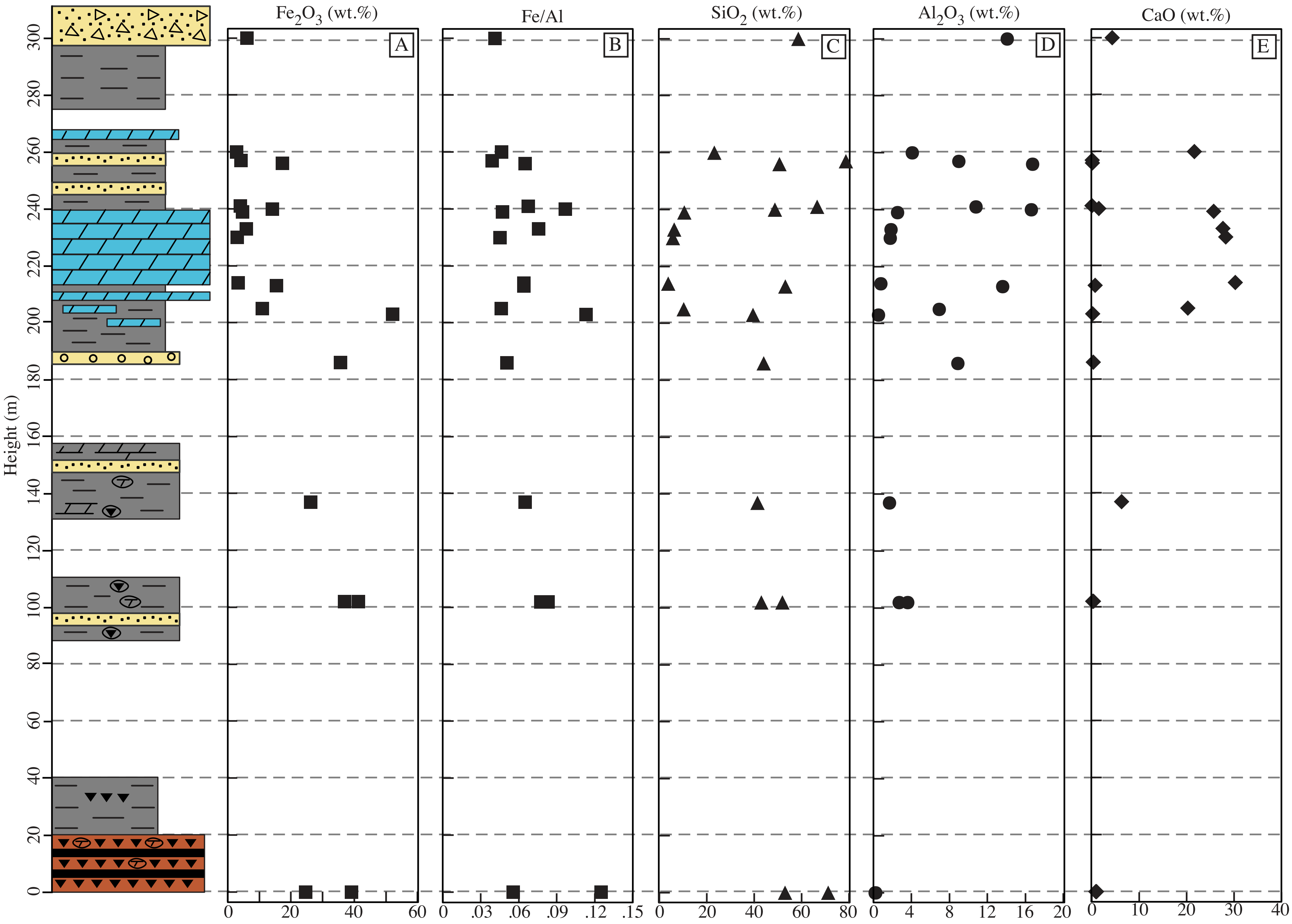

Height (m)
Fe2O3 (wt.%)
Fe/Al
SiO2 (wt.%)
Al2O3 (wt.%)
CaO (wt.%)
A
B
C
D
E

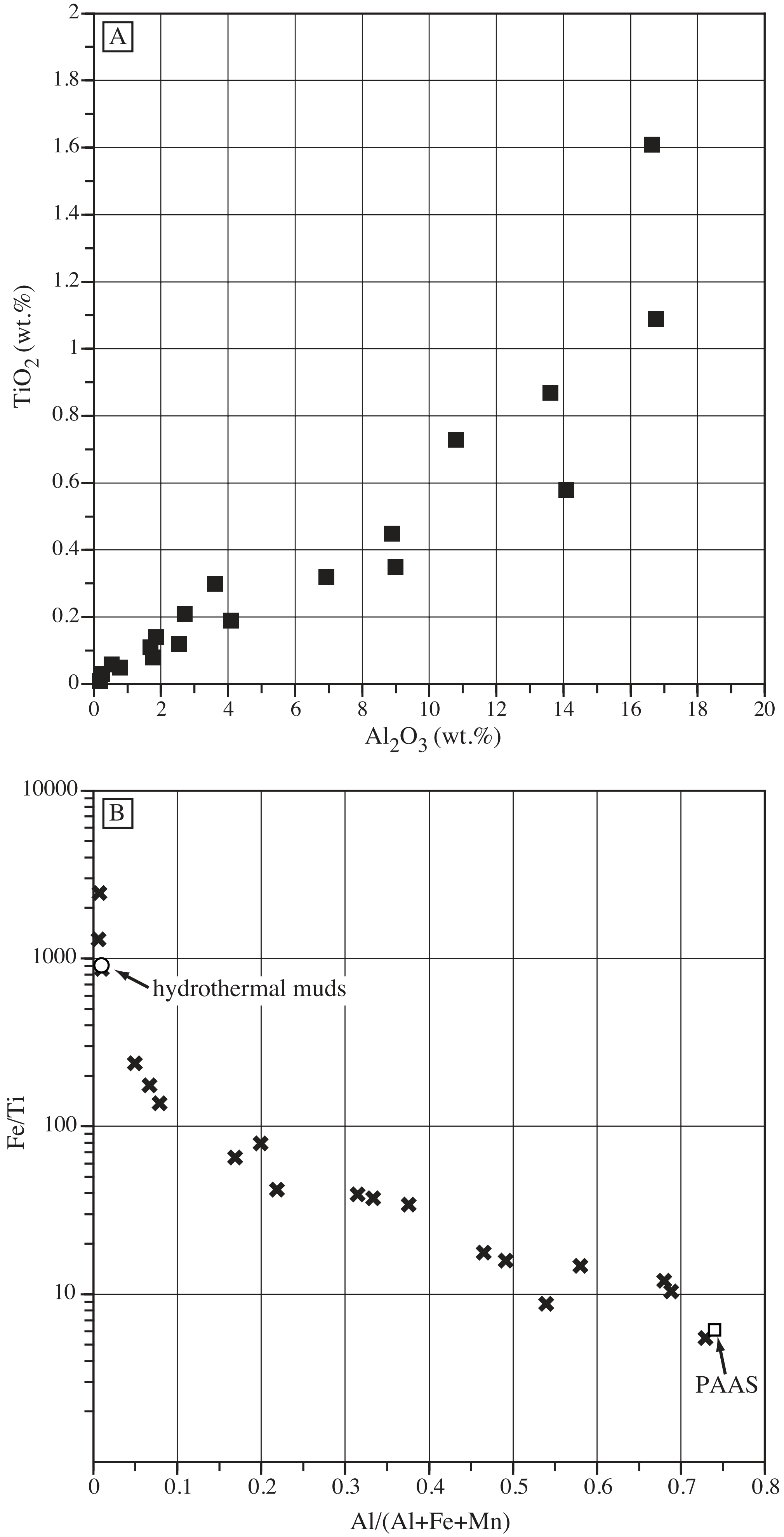
A
TiO2 (wt.%)
Al2O3 (wt.%)
B
Fe/Ti
Al/(Al+Fe+Mn)
hydrothermal muds
PAAS

Figure 7

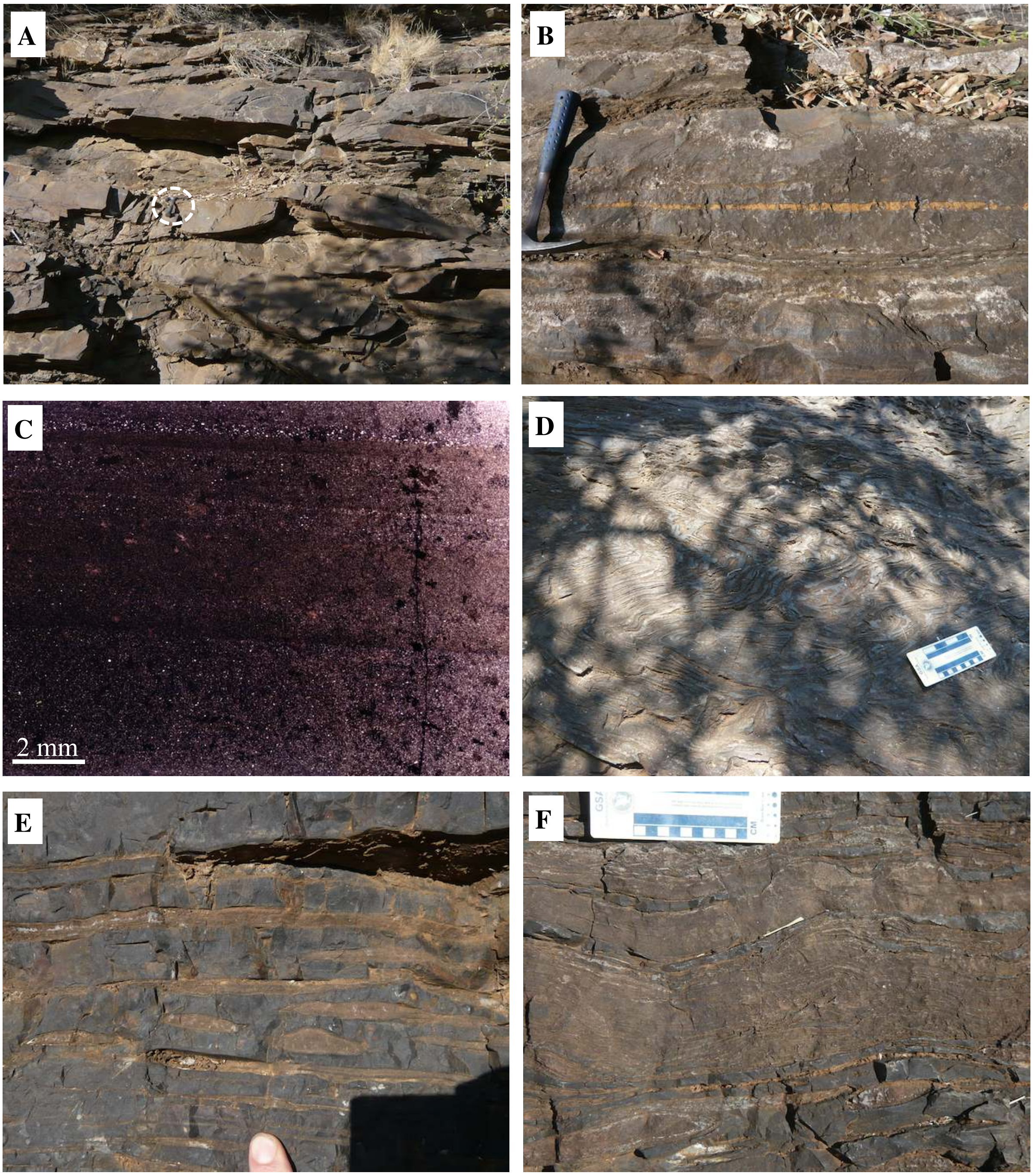

Figure 8

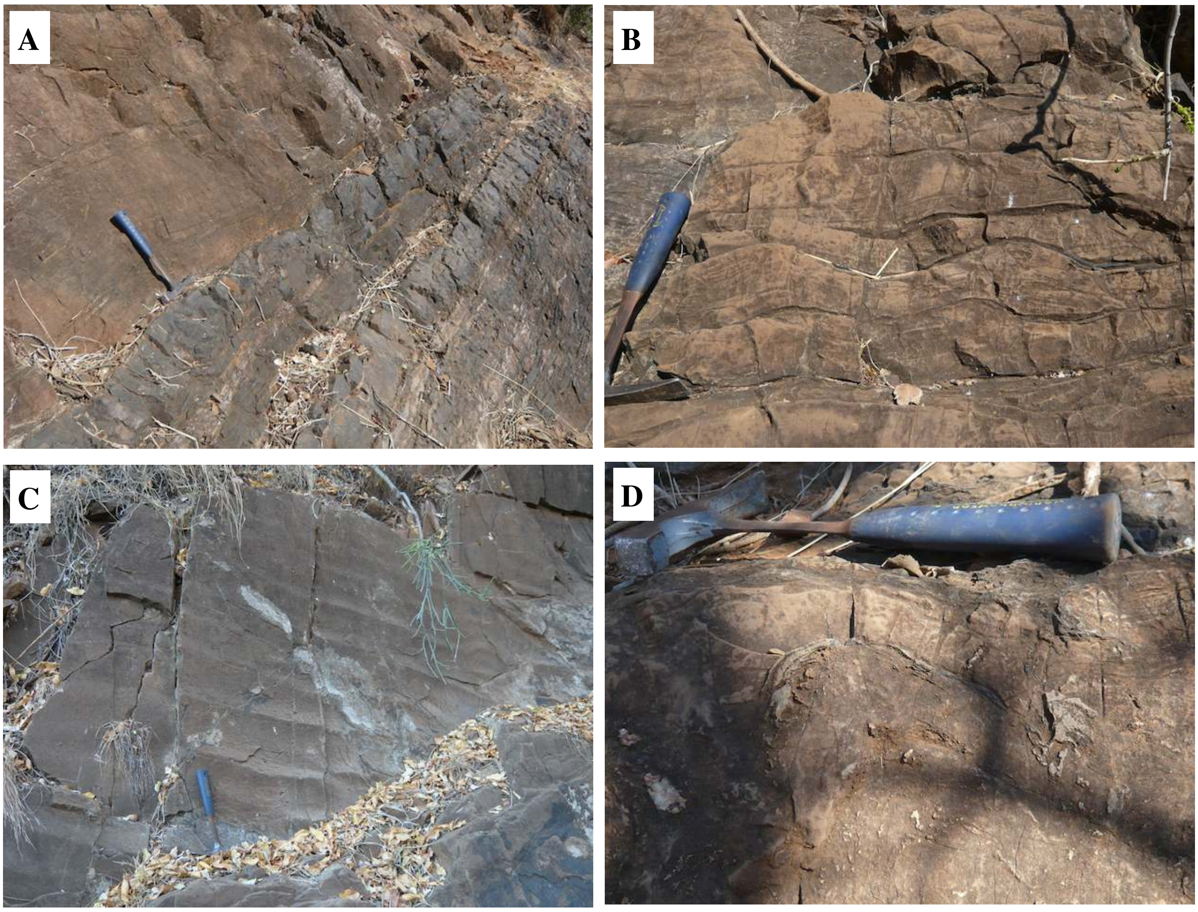

Figure 9

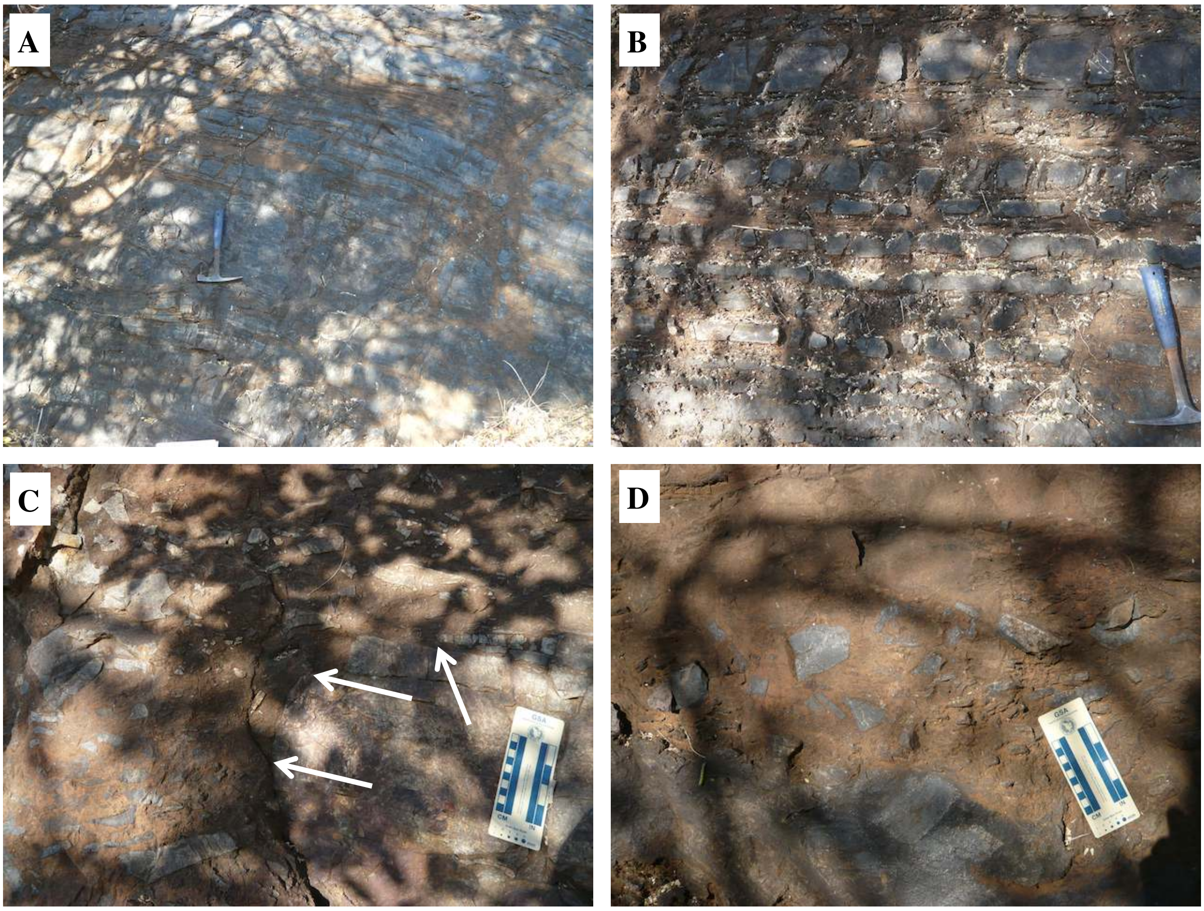

Figure 10

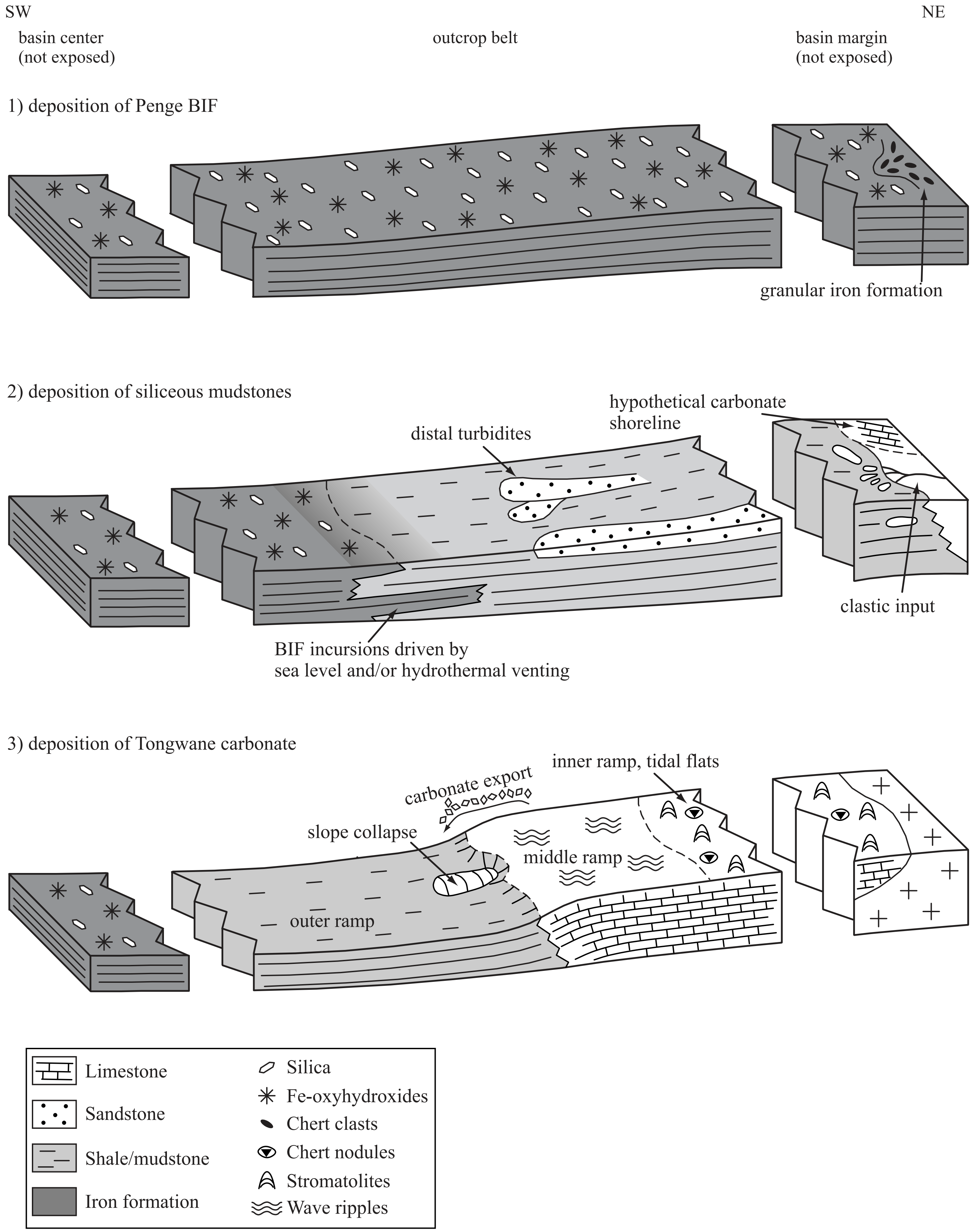
SW
NE
basin center
(not exposed)
outcrop belt
basin margin
(not exposed)
1) deposition of Penge BIF
granular iron formation
2) deposition of siliceous mudstones
hypothetical carbonate
shoreline
distal turbidites
clastic input
BIF incursions driven by
sea level and/or hydrothermal venting
3) deposition of Tongwane carbonate
inner ramp, tidal flats
carbonate export
slope collapse
middle ramp
outer ramp
Limestone
Sandstone
Shale/mudstone
Iron formation
Silica
Fe-oxyhydroxides
Chert clasts
Chert nodules
Stromatolites
Wave ripples

Figure 11

Table 1: Mineralogical data.

Sample	Height (m)	Phases identified
To1	**0**	quartz, magnetite, riebeckite
To2	**205**	quartz, dolomite, pyrochlore, chamosite, mica, dravite
To3	**233**	quartz, dolomite, calcite, biotite, clinochlore, huntite, dravite
To9	**214**	dolomite, calcite, biotite, albite
To13	**239**	quartz, dolomite, calcite, biotite, clinochlore, huntite
To14	**240**	quartz, biotite, rutile, orthoclase, muscovite, birnessite
To21	**102**	quartz, biotite, ankerite, haematite, augite, magnetite, grunerite
To23	**137**	quartz, biotite, ankerite, goethite, grunerite
To26	**186**	quartz, biotite, magnetite, grunerite, albite
To29	**260**	quartz, dolomite, calcite, biotite, clinochlore, microcline, albite
To30	**300**	quartz, biotite, ankerite, orthoclase, clinochlore, albite, muscovite

Table 2. Major element data.

Sample	Height (m)	SiO_2	Al_2O_3	TiO_2	Fe_2O_3	MnO	MgO	CaO	Na_2O	K_2O	P_2O_5	Lithology
To1	**0**	53.00	0.24	0.03	39.09	0.03	2.17	0.87	3.64	0.61	0.07	Banded iron formation
To2	**205**	10.30	6.93	0.32	10.96	0.56	16.81	20.25	0.08	0.89	0.11	Dolomite
To3	**233**	6.29	1.85	0.14	5.89	0.72	17.38	27.65	0.08	0.51	0.07	Dolomite
To8	**213**	53.12	13.61	0.87	15.43	0.23	5.74	0.73	0.35	6.75	0.14	Mudstone
To9	**214**	3.77	0.78	0.05	3.27	0.57	18.43	30.25	0.06	0.16	0.04	Dolomite
To12	**230**	5.75	1.77	0.08	2.99	0.55	17.74	28.24	0.05	1.16	0.05	Dolomite
To13	**239**	10.55	2.54	0.12	4.73	0.80	15.89	25.70	0.04	0.75	0.04	Dolomite
To14	**240**	48.73	16.63	1.61	14.15	0.05	3.05	1.51	0.08	10.42	0.14	Mudstone
To15	**256**	50.65	16.76	1.09	17.32	0.04	3.45	0.15	0.07	8.02	0.11	Mudstone
To16	**257**	78.64	8.99	0.35	4.22	0.01	1.10	0.11	0.04	4.19	0.04	Litharenite
To17	**420**	49.27	13.84	0.94	11.96	0.19	1.69	8.62	1.76	1.15	0.19	Dolerite
To18	**0**	71.18	0.18	0.01	24.61	0.35	1.59	1.02	0.17	0.38	0.01	Banded iron formation
To21	**102**	51.89	2.71	0.21	36.95	0.90	4.02	0.21	0.21	2.24	0.07	Ferrugenous mudstone
To22	**102**	43.01	3.61	0.30	41.27	0.90	4.79	0.38	0.19	2.93	0.12	Mudstone
To23	**137**	41.39	1.69	0.11	26.19	6.34	3.75	6.30	0.02	1.20	0.11	Mudstone
To26	**186**	44.01	8.89	0.45	35.69	0.05	4.99	0.34	1.27	3.45	0.10	Mudstone
To28	**203**	39.50	0.53	0.06	52.11	0.24	6.08	0.21	0.04	0.19	0.04	Mudstone
To29	**260**	23.20	4.09	0.19	2.81	0.15	14.21	21.63	0.04	2.74	0.05	Stromatolitic dolomite
To30	**300**	58.60	14.09	0.58	6.04	0.34	5.34	4.32	1.20	5.55	0.14	Diamictite
To31	**241**	66.53	10.80	0.73	4.01	0.00	0.11	0.06	0.08	9.37	0.11	Litharenite

Table 3: Facies observations and interpretations.

Facies	Observations	Interpretation
Banded iron formation	Macrofacies: very regular dm- to cm-scale interbedding of Fe oxides, chert, siderite; individual beds with internal lamination; local cm-scale nodules of siderite/sideritic chert. Microfacies: sub-mm to mm-scale alternation of chert and Fe-oxides, the latter partially replaced by riebeckite with tabular to acicular crystal habits (crystal size mostly ~500μm, locally <1100μm). Mineralogy: chert 11.3vol.%, Fe-oxides 13.7vol.%, riebeckite 75vol.%.	Below storm wave base. Hydrothermal source of Fe. Metamorphic alteration of Fe-oxides to riebeckite.
Shale	Macrofacies: black weathering, dark grey to black on fresh surfaces; regular thin beds weathering in a characteristic blocky-tabular nature; very localized cm-thick interbeds and nodules of ferruginous dolomite and chert.	Below storm wave base.
Siliceous mudstone and shale	Macrofacies: irregular-nodular weathering with stronger silicification, thick to thin bedded; interstratified cm and dm-thick shale horizons; local mm- and cm-scale nodules and beds of yellow-brown ferruginous dolomite; interbedded mm-scale alternations of chert, Fe-oxides, riebeckite, and ankerite at 88-110m of section are similar to BIF. Microfacies: fine-grained angular detrital quartz in mm-thick lamiane and clay minerals (commonly metamorphosed to biotite); metamorphic grunerite locally obscures depositional microtextures.	Below storm wave base. Clastic input (gravity deposits). Metamorphic overprint: biotite, grunerite.
Siliceous mudstone and shale with dolomite interbeds and nodules	Macrofacies: shales/siliceous mudstones thinly interbedded with bands (>10cm wide, ~1cm thick) and pre-compactional nodules (average diameter 3-5cm) of dolomite; dolomite usually makes up about 20% of thickness, but locally can reach 50%; dolomite weathers red-brown and yellowish-brown, medium grey on fresh surfaces; some dolomites with flat and wavy lamination; slump structures common (1-2m in scale). Microfacies: dolomite composed of dolo-microspar (<30µm), immature stylolites with euhedral cubic pyrite crystals, largely free of clay minerals and biotite; grunerite formation in non-carbonate facies (22-36vol.%).	Below storm wave base. Increasing carbonate export and/or in-situ precipitation. Gravity-driven processes on slope.
Dolomite with mudstone seams	Macrofacies: thin and thick bedded; 60% of thickness are laterally persistent cm- and dm-thick dolomite beds; domal structures are possibly stromatolites and/or slumps; local beds of siliceous mudstone up to 20cm thick (2 prominent beds near the top of unit). Microfacies: mudstone layers 10-12mm thick, interbedded with xenotopic dolo-microspar (crystals <30µm; locally recrystallized <460μm along interface of both lithologies).	Below storm wave base. Carbonate export and benthic precipitation. Gravity-driven processes on slope.
Massive dolomite	Macrofacies: red-brown to yellowish-brown weathering, fresh surfaces medium-grey; thick bedded with undulating bed contacts, local shale seams; flat to wavy lamination and wave ripples (paleo-azimuths between 120° and 130°), very localized hummocky cross-stratification; crinkly lamination and cm-scale domal stromatolites near top; cm-scale chert nodules increase towards the top, commonly trace stromatolite lamination. Microfacies: xenotopic dolomite (crystals <100µm); stylolites are often overprinted by euhedral pyrite. Mineralogy: dolomite 91-97vol.%, detrital quartz and feldspar 1-2vol.%, biotite and other metamorphic (sheet) silicates (e.g. muscovite, chlorite, and clinochlore) detected in XRD, but are very minor phases (1-5vol.%), pyrite ≤1vol.%.	Shallowing from storm-wave base to above fair weather wave-base. Middle to inner ramp.
Sandstone, conglomerate	Sandstone beds 2-3mm thick, but occur stacked over several cm to dm of stratigraphic thickness; planar laminated fine-grained sandstones (grain size 50-100µm), fining upwards through silt to mud. Single chert conglomerate, few cm thick, clast-supported, poorly sorted, granule to fine pebbles (diameter up to 8mm).	Sandstone: distal turbidites. Conglomerate: turbidite, debris flow.